To cite this version :

El Hachemi AMARA, K KHELOUFI, T TAMSAOUT, Rémy FABBRO, Koji HIRANO - Numerical investigations on high-power laser cutting of metals - Applied physics. A, Materials science & processing - Vol. 119, p.1245-1260 - 2015

Numerical investigations on high-power laser cutting of metals

E. H. Amara[1] · K. Kheloufi[1] · T. Tamsaout[1] · R. Fabbro[2] · K. Hirano[3]

Abstract A theoretical approach based on a numerical simulation using experimental data is proposed as a contribution for the study of laser metal cutting under gas assistance. The aim is to simulate the stages of the kerf formation by considering the induced generated melt film dynamics, while it interacts with the laser beam and the assisting gas jet. For normal atmospheric conditions, a 3D model is developed using the finite volume method to solve the governing hydrodynamic equations, supplied with the species conservation equation. The present air, the metallic liquid, and the solid metal are considered as phases, where the interface positions are tracked by implementation of the volume-of-fluid method through Fluent CFD code, whereas an enthalpic method is used to take into account the material melting and resolidification. The results for six operating conditions in relation to the cutting velocity show an interesting agreement with the experimental observations.

1 Introduction

Due to its speedness, repeatability, and reliability for a wide range of material types, laser cutting is considered as one of the most important laser material machining processes. Dahorte and Harikmar [1] described four main techniques for cutting material by laser: the evaporative laser cutting, the fusion cutting, the reactive fusion cutting, and the controlled fracture technique. Depending on the operating conditions, the optimum technique can be chosen. The approaches that should be adopted to process materials with low and high conductivity such as clothes and metals are presented by Ready [2], where the direct vaporization by laser energy with nonreactive gas jet should be used for cloth, but for a metal such as titanium, exothermic reaction with oxidizing gas should be considered, whereas for stainless steel, a nonreactive gas jet can be used to blow out the molten material. The laser beam can be used for fusion cutting either by only melting a thin material film or by melting and vaporizing it, resulting in narrow and clean-cut widths produced on quite large depths. As shown in Fig. 1, the molten film is expelled from the cutting front by directing a pressurized assist gas jet usually issued from a coaxial nozzle. The cut can be obtained either by moving the laser beam across the sample surface, or by moving the workpiece while the cutting device delivering the laser beam and the gas jet is kept fixed.

Although laser cutting process is nowadays widely used in miscellaneous industries involving metals, ceramics, and processing, important issues are still raised, mainly concerning the defaults issue where striations and dross resulting in the cut product, which constitute the main disadvantage of laser cutting. The physical mechanisms occurring during laser cutting and their influence on the cut quality are thus currently investigated by both experimental and theoretical approaches, with the aim to get a better comprehension on the governing phenomena and subsequently to act by controlling the operating parameters toward enhancing the cutting product quality. The

✉ E. H. Amara
amara@cdta.dz

1 Laser Material Processing Team, Centre de Développement des Technologies Avancées, PO Box 17, Baba-Hassen, 16303 Algiers, Algeria

2 Laboratoire Procédés et Ingénierie en Mécanique et Matériaux, Arts et Métiers ParisTech - 151 bd de l'Hôpital, 75013 Paris, France

3 Nippon Steel Corporation, Marunouchi Park Building, 2-6-1 Marunouchi, Chiyoda Ward, Tokyo 100-8071, Japan
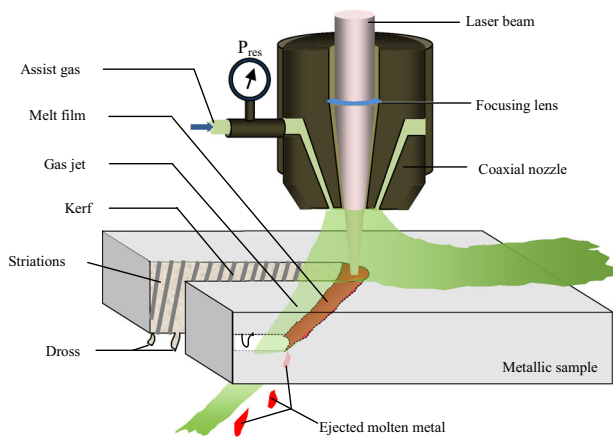
Fig. 1 Schematic representation of laser cutting principle

elimination or the reduction of the undesirable effects is the main goal of the studies developed on laser cutting.

Since the 1980s, many authors proposed models to understand the basic physical phenomena and the involved mechanisms, with the aim to model and to simulate the melt behavior and its free interfaces. Schuocker [3] has developed a theoretical model to study the dynamic behavior of the cutting process based on a concept of global mass and energy balance, with a small perturbation treatment for the differential balance equations. Schuocker and Muller [4] have moreover theoretically shown that the liquid layer can oscillate with a natural frequency, prior to its ejection out of the bottom of the kerf. The results obtained for the natural frequency have correlated reasonably with experimental work. It does not however explain why striations are much more pronounced in reactive gas-assisted laser cutting than in inert gas cutting. Schulz et al. [5] developed a simplified two-dimensional model based on energy balance to examine the effect of laser beam parameters such as laser intensity and polarization on thin melted film. Vicanek and Simon [6] proposed that the ejection of melt from the laser cut kerf is mainly driven by two forces exerted by the assist gas jet which includes: the frictional force at the gas/melt interface and the pressure gradient. They concluded that both contributions are of the same orders, and these two strengths increase with increasing velocity of the gas jet and with that of the angle of inclination of the kerf. In another model proposed by Vicanek et al. [7] for film flow stability to investigate the dynamic behavior of the molten layer, it was shown that the stationary solution is dependent on cutting speed, but the energy equation was not discussed and the convective term in the momentum equation was omitted. A model for laser fusion cutting was presented by Petring et al. [8], where the beam parameters and the Fresnel absorption were considered for the calculation of a three-dimensional stationary cutting front, based on the assumption that the width of the cutting front is identical to

the laser beam diameter and that the angle of the inclined front is constant throughout the depth of the cut. Schulz and Becker [9] developed a numerical iterative approach, which was used to calculate the three-dimensional cutting front geometry. Makashev et al. [10] proposed a quantitative physical model to investigate the evolution of a small perturbation created on a two-dimensional kerf front. It was expressed on the basis of the local drilling velocity, which depends on the local laser absorbed intensity and on the local inclination angle of the kerf front. In another paper, Makashev et al. [11] proposed an estimation of roughness parameters of the cut walls, with the pressure and velocity distribution over the cutting front. Kaplan [12] proposed a simple analytical model for laser cutting with oxygen and inert assist gases. It was described by using a set of balance equations for mass, momentum, and energy to calculate temperature, melt film velocity, and film thickness. However, due to the simplification of the momentum equation, the model could not be used to explain the dynamic behavior of the process. Yilbas [13] developed a mathematical modeling of CO_2 laser cutting, where a numerical solution of the heat transfer equation has been obtained, and the melting front velocities for different laser beam powers and workpiece thicknesses have been predicted. Tani et al. [14] proposed an analytical model in which, by considering mass, force, and energy balances and that the kerf is half-moon shaped, the geometry and temperature fields of the melt film have been evaluated. Golubev [15] developed a study for the melt removal mechanisms during material laser cutting under gas assistance. The paper discussed and revised earlier proposed mechanisms describing striation formation and also reported on the mechanism of moving humps on the melt layer for given cutting velocities, which gives rise to striations as well. Theoretical and experimental approaches on CO2 laser cutting of metallic substrate were developed by Yilbas and Abdul Aleem [16] in their study on the dross ejection. It was concluded that the laser power and the assisting gas jet intensities have an effect on the liquid layer thickness and subsequently on the droplet formation. Wee et al. [17] studied the effects of the interaction time, the irradiance, the assist gas pressure on the laser cutting quality of alumina, the striation angle and wavelength, and the distance of clearly defined striations. Rajpurohit and Patel [18] proposed a review on the striation mechanism which affects the quality of laser cutting and the associated quality improvement techniques. In another study on dross formation, fiber laser cutting of stainless steel was considered by Teixidor et al. [19]. They have investigated for fixed gas type and pressure the effect of the pulsed laser parameters (peak power, frequency) and the cutting speed, and it was concluded that by using suitable parameters, fiber lasers could be the solution to obtain dross with reduced dimensions.

In the most of the proposed models, it appears that the results were derived from pre-assumed geometrical kerf shapes, since the cutting front is generally taken to be a semicircle due to the rotationally symmetrical laser beam. Stationary approaches that ignore the dynamical nature of the process are used. In other models, the kerf width is generally assumed to be constant through the depth of the cut. A numerical simulation model for laser material processing has been proposed by Otto et al. [20], where the authors used the OpenFOAMR software. They have noted that the external gas jet simulation is quite challenging as it is necessary to model the compressible gas flow. Recently, Kohl and Schmidt [21] refined the model and applied it for laser cutting, where the gas jet was represented by applying the pressure directly at the upper boundary.

In our contribution, we develop a numerical study with the aim to simulate the occurring phenomena when a sample is moved under a laser beam, and to obtain a cutting kerf at given laser operating parameters, under normal atmospheric conditions. A 3D modeling is conducted by implementing the finite volume method through Ansys-Fluent CFD softwares to solve the hydrodynamic governing set of equations. The volume-of-fluid (VOF) method is applied for liquid–gas interfaces tracking, and suitable boundary conditions and source terms are introduced in the Fluent calculation process. By solving the unsteady Navier–Stokes, energy, and the VOF equations, we obtain the kerf profile formation, and we observe the generated periodical movement (humps) on the cutting front for given process velocity conditions. The model involves the implementation of a local absorbed laser intensity depending on the tilt angle. At low cutting speeds, the shelf structure formation is obtained by using our model, in accordance with the experimental observations of Hirano and Fabbro [22], and as predicted by Golubev [15]. The main data used in the simulation concern the temperature-dependent physical properties of the workpiece, the laser beam parameters, and the surrounding air conditions. A quite complex problem is thus considered, where standard feature of the CFD Fluent code must be enhanced, and for that, we have developed numerical procedures called user-defined functions (UDF), working interactively with Fluent in order to solve numerically the governing equations.

2 Mathematical modeling

As represented in Fig. 2, a multiphase problem is considered for the following three involved phases: the surrounding air, the solid workpiece, and the molten part of the workpiece. The both phases of the workpiece (solid and metallic liquid) are assumed as fluids, since the
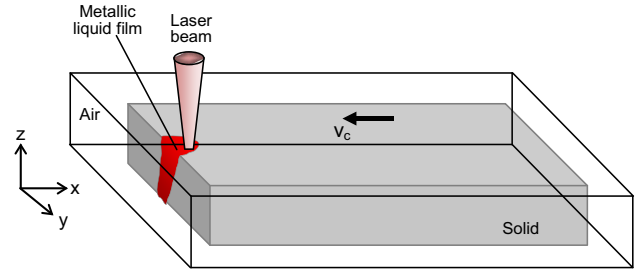
Fig. 2 Representation of the workpiece surrounded by air. The laser beam is displaced over the sample surface

implemented VOF method for interface tracking considers only the interaction between different fluids.

The VOF method was for the first time introduced by Hirt and Nichols [23] in a code called SOLA-VOF for material interface tracking inside an Eulerian grid. The method is related to the resolution of Euler or Navier–Stokes equations by finite difference or finite volume schemes. The principle of the interface tracking is to determine the fluid quantity in each control-volume (cell) by evaluating a quantity called volume fraction. When the volume fraction is equal to 1, then the cell is full of fluid, and if it is equal to 0, the cell is either empty or filled by another fluid.

For the assumed experimental data of Hirano and Fabbro [22] used as operating parameters in our modeling, a Newtonian and laminar flow involving a free surface deformation is considered for the liquid metal. A model is developed to solve the set of hydrodynamic equations which govern the melt film dynamics during the interaction with the absorbed laser beam and the gas jet, under normal atmospheric conditions.

2.1 The laser absorbed energy

The effect of laser light interaction with given material depends on the thermal and optical properties of the targeted material and on the used laser beam characteristics. Among the main properties, the thermal diffusivity κ, the absorption coefficient α, and the reflectivity R are determined for the material response to the laser deposited energy at the workpiece surface, beside the effect of the laser beam wavelength λ, its interaction time or pulse duration τ, its energy density or fluence, its divergence, its mode, its polarization, etc. The material electrons absorb the photon energy $E = hc/\lambda$, when it is higher then the binding energy of the material atoms. The absorbed energy is redistributed in the lattice, where the initiated molecular agitation leads to temperature growing, and then a layer of given thickness is affected, leading to fusion and vaporization. When the interaction time is relatively higher, thermal vaporization is obtained on metallic targets, for infrared or ultraviolet

wavelengths. In our model, a top-hat laser beam profile is considered, where the power density Q_{abs} (W/m³) describing the absorption of the incident radiation obeys to the Beer–Lambert law given by:

$$Q_{abs}(z) = \alpha I_o (1 - R(\theta)) \cos(\theta) e^{-\alpha(\lambda)z} \qquad (1)$$

where Q_{abs} is the power density absorbed at given depth z, I_o the incident laser irradiance (W/m²), α the absorption coefficient (m⁻¹), $R(\theta)$ the material reflectivity for the considered wavelength, and θ the laser beam incidence angle on the sample surface. The reflectivity can be deduced from its relation with the refraction and the extinction indices which depend on the material optical properties related to the used laser wavelength. It is given by:

$$R = \frac{(n-1)^2 + k_e^2}{(n+1)^2 + k_e^2} \qquad (2)$$

By considering the effect of the polarization state for the cutting process, we can write from Fresnel's relations the reflectivities of parallel and perpendicularly polarized radiation such as:

$$R_P = \frac{(n \cos\theta - 1)^2 + (k_e \cos\theta)^2}{(n \cos\theta + 1)^2 + (k_e \cos\theta)^2} \qquad (3)$$

$$R_S = \frac{(n - \cos\theta)^2 + k_e^2}{(n + \cos\theta)^2 + k_e^2} \qquad (4)$$

Zaitsev et al. [24] investigated the effect of polarization of a Gaussian beam on the radiation absorption during laser cutting of metals. It was shown that the cutting of materials by the TEM_{00} beam is most efficient when the beam has elliptical polarization directed along the direction of beam displacement and characterized by a specific axial ratio.

The averaged absorptivity for a nonpolarized beam for an opaque material is thus given by:

$$A = 1 - R_{Ave} \qquad (5)$$

$$\text{where } R_{Ave} = \frac{R_P + R_S}{2} \qquad (6)$$

For an iron sample and a laser beam wavelength of 1.06 μm, the corresponding photon energy is 1.166 eV, which corresponds to a refraction index $n = 3.33$ and an extinction coefficient $k_e = 4.52$. These values are deduced from the handbook edited by Lide [25], concerning the iron optical properties at the considered wavelength.

Whereas the laser wavelength-dependent absorption coefficient α is given by:

$$\alpha = \frac{4\pi k_e}{\lambda} \qquad (7)$$

The laser light penetrates the material over a thickness $z_o = 1/\alpha(\lambda)$, where the electromagnetic radiation is reduced by a factor 'e' over a distance called 'skin depth,' given by

$d = \lambda/2\pi k_e$. We define the molten thickness $z_1 = (\kappa\tau)^{1/2}$, where τ is a characteristic laser beam interaction time duration, as a function of the thermal diffusivity $\kappa = k/\rho C_p$, where k is the material thermal conductivity coefficient, ρ its density, and C_p its thermal capacity. Thus, the electromagnetic wave interacts with a layer of thickness z_o and affects a layer of thickness z_1. We note that for metallic targets, the ratio between the heat-affected thickness and the layer penetrated by the laser beam is about 50. Whereas for dielectric materials, κ is clearly smaller than for metallic materials, and thus z_1 is close to z_o. In such situation, we must consider that in our case, when a powerful laser beam impinges on a metallic surface, it interacts with an extremely small skin depth, and thus we can assume that the laser beam energy is deposited at the air–material interface.

In order to deal with the effect of the continuous interface deformation occurring at given cutting velocity regimes, on the amount of the laser absorbed energy, it is important to calculate the incidence angle θ at each area reached by the laser beam in order to obtain the accurate absorbed energy at the interface between the workpiece and the air. In the case of our calculation field, where the sample is surrounded by air, this interface cannot be represented by a boundary, since it constitutes an internal region inside the calculation domain. The VOF method allows us to make difference between the cells containing air and those containing liquid or solid. On the workpiece surface, as shown in Fig. 2, the laser energy is deposited at the material/air interface. The relation between the normal at the interface and the gradient of the volume of the fluid fraction is used to deduce the incidence angle θ over the illuminated region. The approach is close to that proposed by Brackbill et al. [26] (1992) in the continuum surface force model (CSF), where the surface curvature is computed from local gradients in the surface normal at the interface. The $\cos(\theta)$ given in the Eq. (1) is thus obtained from the ratio of the z component gradient of the fluid fraction F to its magnitude gradient which is related to the normal of the workpiece surface and then to the incidence angle such as:

$$\cos(\theta) = \frac{\vec{\nabla} F_z}{\left| \vec{\nabla} F \right|} \qquad (8)$$

The VOF variable F will be developed in Sect. 2.3. The calculation of the tilt (incident) angle during the cutting process, following the interface deformation, is obtained for the different cases of the liquid–air interface inclination as shown in Fig. 3.

The relative displacement effect of the laser beam and the energy deposition on the kerf wall is inserted into the governing equation as source terms through UDFs.
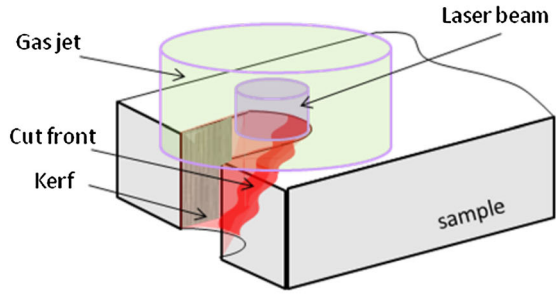
Fig. 3 Laser energy distribution on the cutting front

2.2 The gas jet

The other important parameter in laser cutting is the supplied gas jet used to blow away the molten material film, allowing the kerf development and maintaining it open. The gas pressure can be expressed from the Bernoulli equation in compressible case such as:

$$\frac{\gamma}{\gamma-1}\frac{P_{\text{tot}}^{(\gamma-1)/\gamma}}{\rho_g P_o^{-1/\gamma}} = \frac{\gamma}{\gamma-1}\frac{P_{\text{in}}^{(\gamma-1)/\gamma}}{\rho_g P_o^{-1/\gamma}} + \frac{1}{2}v_g^2 \tag{9}$$

where γ is the ratio of the specific heats (C_p/C_v), P_{tot} the pressure inside the supplier tank, ρ_g the gas density, v_g its velocity at the nozzle exit, P_o the ambient pressure (101,325 Pa), and P_{in} the static pressure which is estimated from the Bernoulli equation. The pressure in the kerf is a combination of the static and the dynamic pressures, where the gas flow can be controlled by acting both on the total gas pressure and the nozzle outlet diameter. In our model, for the considered operating parameters, we use the gas velocity deduced experimentally by Hirano [27], which was directly measured by a Pitot tube. The dynamic pressure is thus obtained and used as a source term in the momentum conservation equation, which represents a part of the gas jet effect on the melt film, the other part being represented by the friction force. The paper of Rasheed [28] gives more details about the control of the gas jet, the type of gas, and the effect of the nozzle standoff distance, as well as the coaxial technique features.

2.3 Melt dynamics governing equations

The transport for the mass, the momentum, the energy is governed by the hydrodynamic conservation equations, supplied with the VOF equation which determines the phase fraction, and the air–material free surface position.

By using the finite volume method implemented by Fluent code, the time-dependent conservation equations solved numerically on all the domains (air, material) are given by:
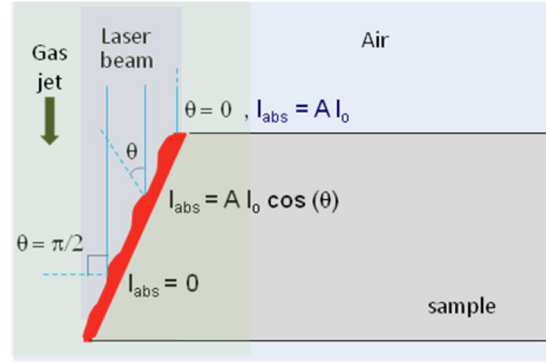
- The volume-of-fluid (VOF) equation:

The VOF variable is calculated from the following conservation equation:

$$\frac{\partial F}{\partial t} + \vec{v} \cdot \vec{\nabla}F = 0 \tag{10}$$

where t is the time and $\vec{v}$ the velocity vector, whereas the VOF variable F varies between 0 and 1. The extreme values 0 or 1 correspond, for the considered phase, to a void or a full cell, respectively, whereas the intermediate values indicate the presence of different phase fractions, which correspond to the free surface elements. Therefore, in order to track the air–workpiece interface, the VOF variable F should be updated at each time step to re-obtain the cells with $\left|\vec{\nabla}F\right| \neq 0$, representing the free surface at the kerf, or the frontier between the air and the material workpiece.

- The continuity equation:

$$\frac{\partial \rho}{\partial t} + \vec{\nabla}(\rho\vec{v}) = 0 \tag{11}$$

where ρ is the density. The incompressibility condition $\left(\vec{\nabla} \cdot \vec{v} = 0\right)$ is assumed for the air by assigning a constant density $\rho = 1.225$ kg/m^3, whereas for the metallic liquid, the solid density is initially assumed, but during the absorption of the laser energy, the density varies with the temperature.

- The momentum equation:

$$\rho\left[\frac{\partial \vec{v}}{\partial t} + \left(\vec{v} \cdot \vec{\nabla}\right)\vec{v}\right] = -\vec{\nabla}p + \mu\Delta\vec{v}$$
$$+ \left(\frac{\partial p_{\text{dyn}}}{\partial z} \cdot \vec{e}_z + \vec{F}_{\text{fric}}\right)\left|\vec{\nabla}F\right| \tag{12}$$

where p is the static pressure, μ is the viscosity, and $\left|\vec{\nabla}F\right|$ denotes the magnitude gradient of the VOF variable F in the tangent plane. Following the previous described papers of Vicanek and Simon [6], and Vicanek et al. [7], the assist

gas jet plays an important role in determining the melt film movements, by supplying two forces due in one part to the dynamic pressure of the gas jet flow given by: $\frac{\partial p_{dyn}}{\partial z} \approx \frac{\Delta p_{dyn}}{d} = \frac{1}{2} \rho_g v_g^2$, where ρ_g and v_g are the gas jet density and its velocity, respectively, d is the workpiece thickness, and $\vec{e}_z$ is the unit vector. In the second part, the force is due to the shear stress resulting from the gas jet viscous friction effect. The gas jet velocity is deduced from the Bernoulli equation, and the gas friction force vector $\vec{F}_f$ acting in the tangential direction of the free surface is given by Vicanek and Simon [6]:

$$\vec{F}_{friction} = 2 \sqrt{\frac{\rho_g \mu_g}{d}} \vec{v}_g^{3/2} \tag{13}$$

where μ_g and d are the gas viscosity and the metal sheet thickness, respectively. The friction force is applied over all the melt film surfaces, and it is obvious that it is easier to deal with the continuous direction of the corresponding friction force vector. Therefore, instead of considering the friction effect of the gas for all the melt surfaces, we assume that the tangential shear stress is only exerted on the central symmetrical line. The corresponding friction force vector components are thus:

$$
\begin{aligned}
F_{x\,friction} &= 2\sqrt{\frac{\rho_g \mu_g}{d}} v_g^{3/2} \cos\theta \\
F_{y\,friction} &= 0 \\
F_{z\,friction} &= 2\sqrt{\frac{\rho_g \mu_g}{d}} v_g^{3/2} \sin\theta
\end{aligned}
\tag{14}
$$

where θ is the incidence angle.

By multiplying the both forces with the gradient of the VOF function for which the nonzero value determines the free surface position, we introduce in the momentum equation the source term due to the gas jet forces.

The term of viscosity μ in the momentum equation is taken constant and equal to 1.7894×10^{-5} kg/m/s for the air region. However, for the material, a fluid state must be considered even for the solid part of the workpiece due to the VOF model requirements. Therefore, a viscosity must be assigned even for the solid part region of the workpiece, and in our model, we have used a temperature-dependent viscosity following Sutherland's viscosity law [29] resulted from a kinetic theory using an idealized intermolecular force potential. The formula is specified using two or three coefficients. In our case, we obtain the following expression:

$$\mu(T) = \mu_{ref} \frac{(T_{ref} + T_{eff})}{(T + T_{eff})} \frac{1}{\sqrt{T/T_{eff}}} \tag{15}$$

where $T_{eff} = 273.11$ K, and for the iron: $T_{ref} = 1800$ K, and $\mu_{ref} = 0.004$ kg/m/s

• The energy equation

As a solidification–melting model is considered, the energy equation is written in the enthalpic formulation. This method makes difference between the heat transfer that is related to phase change through a source term in the energy equation or an equivalent specific heat. It is thus not necessary to calculate explicitly the position of the melt front, and then the same equations are solved in the entire calculation domain, including the solid region, such as:

$$\frac{\partial \rho H}{\partial t} + \vec{\nabla} \cdot \rho \vec{v} H = \vec{\nabla} \cdot \left(k \vec{\nabla} T \right) + S \tag{16}$$

S is a volumetric source term in the energy equation, which corresponds in our case to the laser deposited energy Q_{abs} given in Eq. (1). As proposed by Voller et al. [30], the energy equation is written in such a way that the total energy is separated into two components: the sensible enthalpy heat and the latent heat. The total enthalpy H is given by: $H = C_p T + f_{liq}.L$, where the first term is the sensible enthalpy heat and the second term is the latent heat. C_p is the heat capacity, L the fusion latent heat of the material, and f_{liq} the liquid fraction. As developed by Mazhukin and Samarskii [31], the liquid fraction f_{liq} is assumed to vary linearly with temperature such as

$$
f_{liq} =
\begin{cases}
1 & \text{when} \quad T \geq T_{liquidus} \\
\dfrac{T - T_{solidus}}{T_{liquidus} - T_{solidus}} & \text{when} \quad T_{solidus} \leq T \leq T_{liquidus} \\
0 & \text{when} \quad T \leq T_{solidus}
\end{cases}
\tag{17}
$$

where $T_{liquidus}$ is the temperature at which solid formation commences $T_{solidus}$ the temperature at which full solidification is achieved.

For the treated problem, a volumetric heat flux source representing the absorbed laser energy is automatically applied at the interface between the workpiece and the air region on the kerf cutting front for a nonzero gradient of the VOF variable representing the volume fraction of the material in a computational cell. To consider the interaction with metallic workpiece for which it is well known that the skin depth representing the laser beam penetration is extremely small and thus a superficial absorption should be assumed, the laser absorbed intensity is multiplied with the gradient of F in which the nonzero occurs only in the cells adjacent to the free surface, thus allowing us to have the laser source only applied at the air–metal interface. The energy equation is then written as:

$$\rho C_p \left[\frac{\partial T}{\partial t} + \vec{v}\vec{\nabla}T \right] = \vec{\nabla} \cdot \left(k \vec{\nabla} T \right) - \rho \left[\frac{\partial \Delta H}{\partial t} + \vec{v}\vec{\nabla}(\Delta H) \right] + Q_{abs} \tag{18}$$

Fig. 4 Movement of the workpiece under the laser beam using a moving or a noninertial reference frame
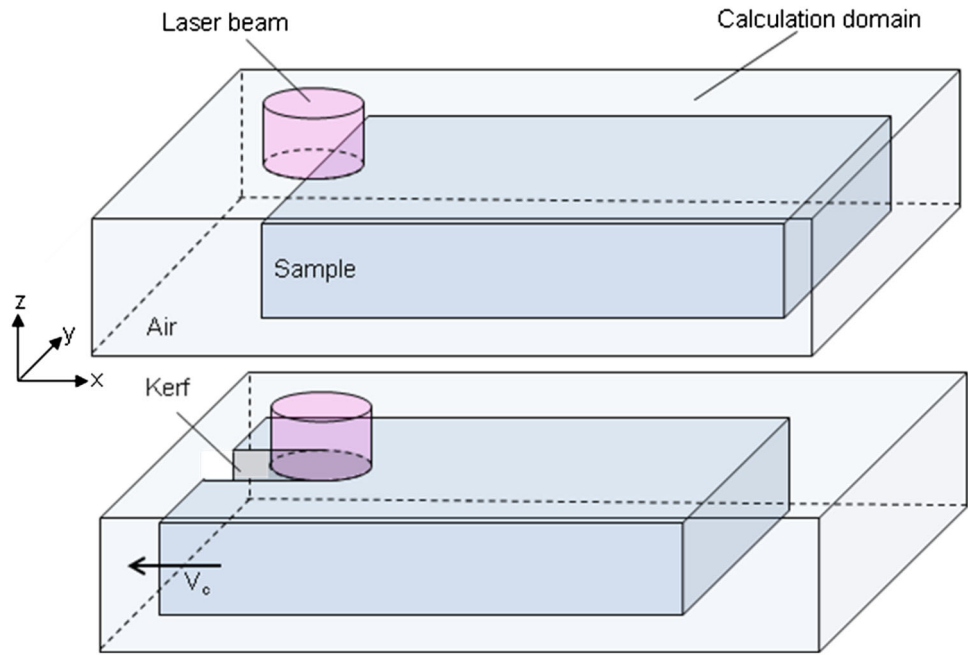
T denotes the temperature, k the thermal conductivity, $\Delta H = \mathrm{f_{liq}} L$ the latent heat, and the source term Q_{abs} representing the absorbed laser energy.

3 Results and discussions

The aim of the developed modeling is to simulate the metallic liquid hydrodynamic movements on the kerf cutting front, under nitrogen (inert) gas jet assistance, at different cutting velocity regimes. In order to compare our numerical modeling results to the experimental observations, we have used operating parameters similar to those used in the experimental work performed by Hirano and Fabbro [22]. The laser parameters, the workpiece, the assist gas characteristics, and the ambient operating conditions are as follows:

- A Nd:YAG laser wavelength 1.06 μm is used as heat source for fusion cutting, and a top-hat laser beam profile is considered.
- The incident laser irradiance I_{o} is related to the laser beam power P and the beam radius r_{l} by the relation: $I_{\mathrm{o}} = 2\,P/\pi r_{\mathrm{l}}^2$. In the performed simulations, $P = 8$ kW and $r_{\mathrm{l}} = 0.8$ mm.
- A 3-mm-thickness iron sample is considered.
- An absorptivity $A = (1 - R_{\mathrm{Ave}})$ depending on incidence angle θ is deduced for the corresponding wavelength and the material (iron) refractive and extinction indices.
- Whereas the absorption coefficient $\alpha = 5.07 \times 10^7$ m^{-1}, which allows us to suppose that the laser energy is absorbed at the metal–air interface.

- In order to compare with the set of experimental results given in Hirano and Fabbro [22], the parametric study concerns cutting speeds from 1 to 6 m/min.
- The inert assist gas is nitrogen with a density equal to 1.3 kg/m^3 and a jet velocity deduced from Eq. (5). As reported by Hirano [27], a turbulent gas jet velocity is calculated to be about 110 m/s, for a corresponding total pressure $P_{\mathrm{tot}} = 2.4$ bar, a static pressure $P_{\mathrm{in}} = 2.1$ bar, and an ambient pressure $P_{\mathrm{o}} = 1$ bar. The deduced dynamic pressure is inserted as a source term $P_{\mathrm{dyn}} = 0.5\,\rho_g v_g^2$ in the Eq. (12).
- The ambient conditions are represented by surrounding air at a temperature of 300 K and a pressure of 101,325 Pa (=1 bar).
- The used viscosity that is considered to vary with the temperature, as given by Sutherland's Eq. (15), allows us to take into account the presence of the solid phase with a viscosity equal to 0.014 kg/m/s, whereas it drops to 0.004 kg/m/s for the iron liquid phase at $T = 1808$ K.
- It is assumed that for the previous operating parameters, there is no generation of vapor or plasma.

The iron sample physical properties (density ρ, heat capacity C_{p}, thermal conductivity K) are considered to be dependent on the temperature, and they are inserted interactively in the calculation process performed by Fluent by using UDFs. In order to take into account the effects of latent heat on the temperature distribution which can be approximated by increasing of the specific heat capacity, the used heat capacity is derived from writing the expression given by Toyerskani et al. [32], as a two order polynom which is a suitable form to be inserted in Fluent
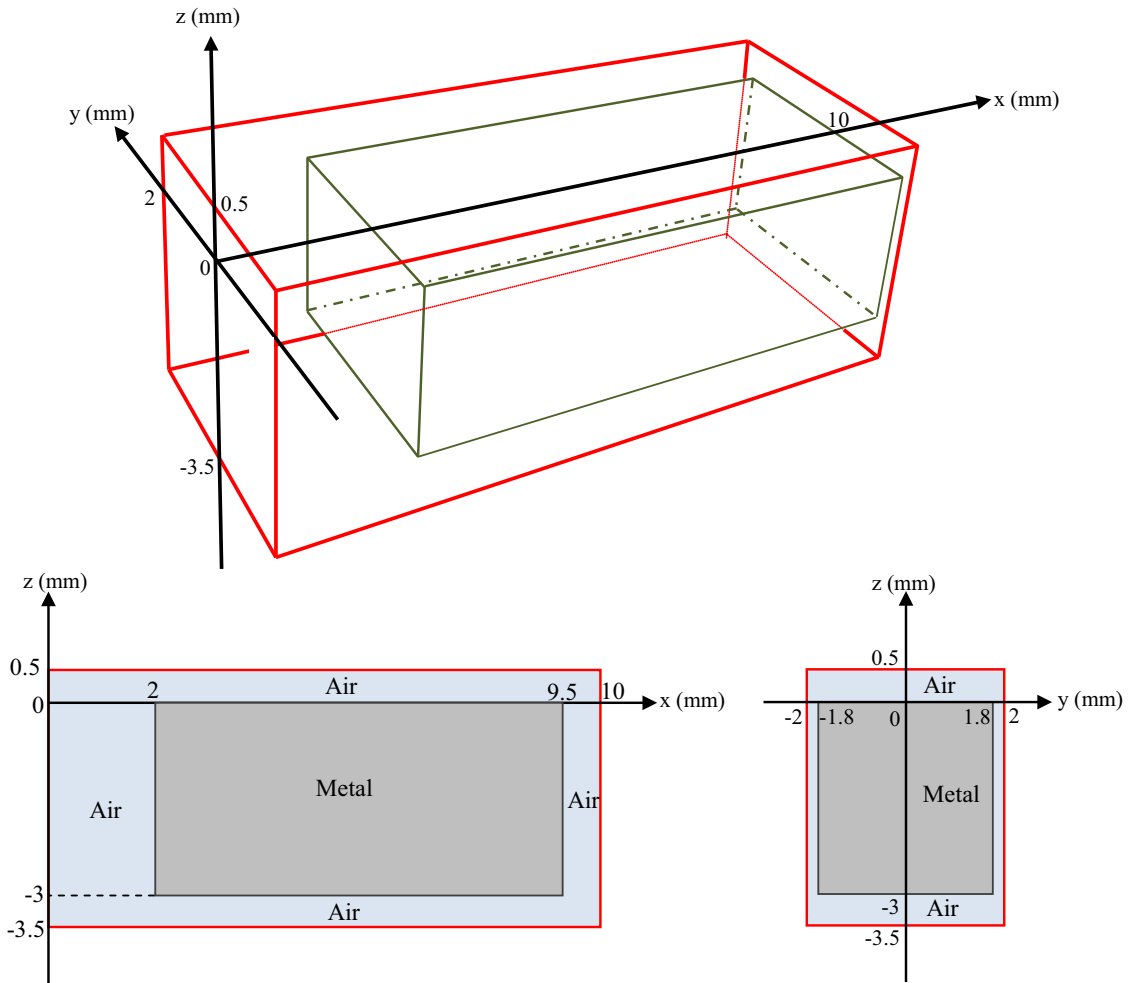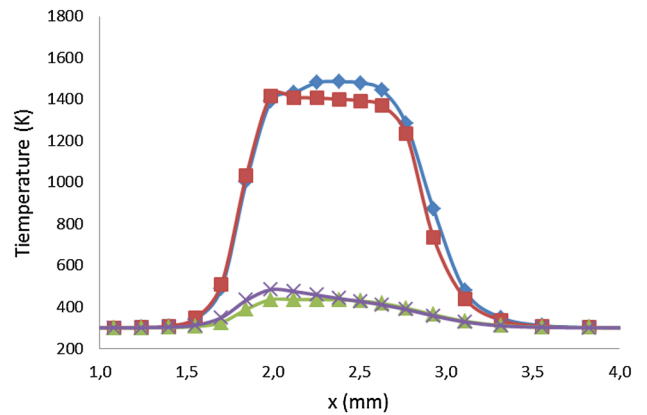
Fig. 5 Calculation field dimensions
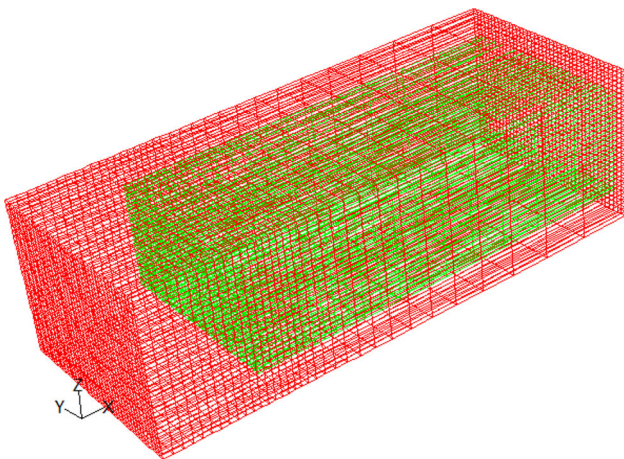
**Fig. 6** Calculation domain mesh

Fig. 7 Grid influence

calculations, whereas the heat conductivity and subsequently the density are derived from Duley [33] who gave tables of temperature-dependent thermal conductivities, and diffusivities for different materials, and from Lampa et al. [34] who considered a thermal conductivity in the case of a stationary melt and an artificial enhanced thermal conductivity induced by thermocapillary flow. The following temperature-dependent equations are thus considered for the iron sample physical properties.

Fig. 8 Experimental
observations and the
corresponding numerical model
results for different cutting
velocities: **a** 1 m/min,
b 2 m/min, **c** 3 m/min,
d 4 m/min, and **e** 6 m/min

1 m/min

2 m/min

3 m/min

4 m/min

6 m/min
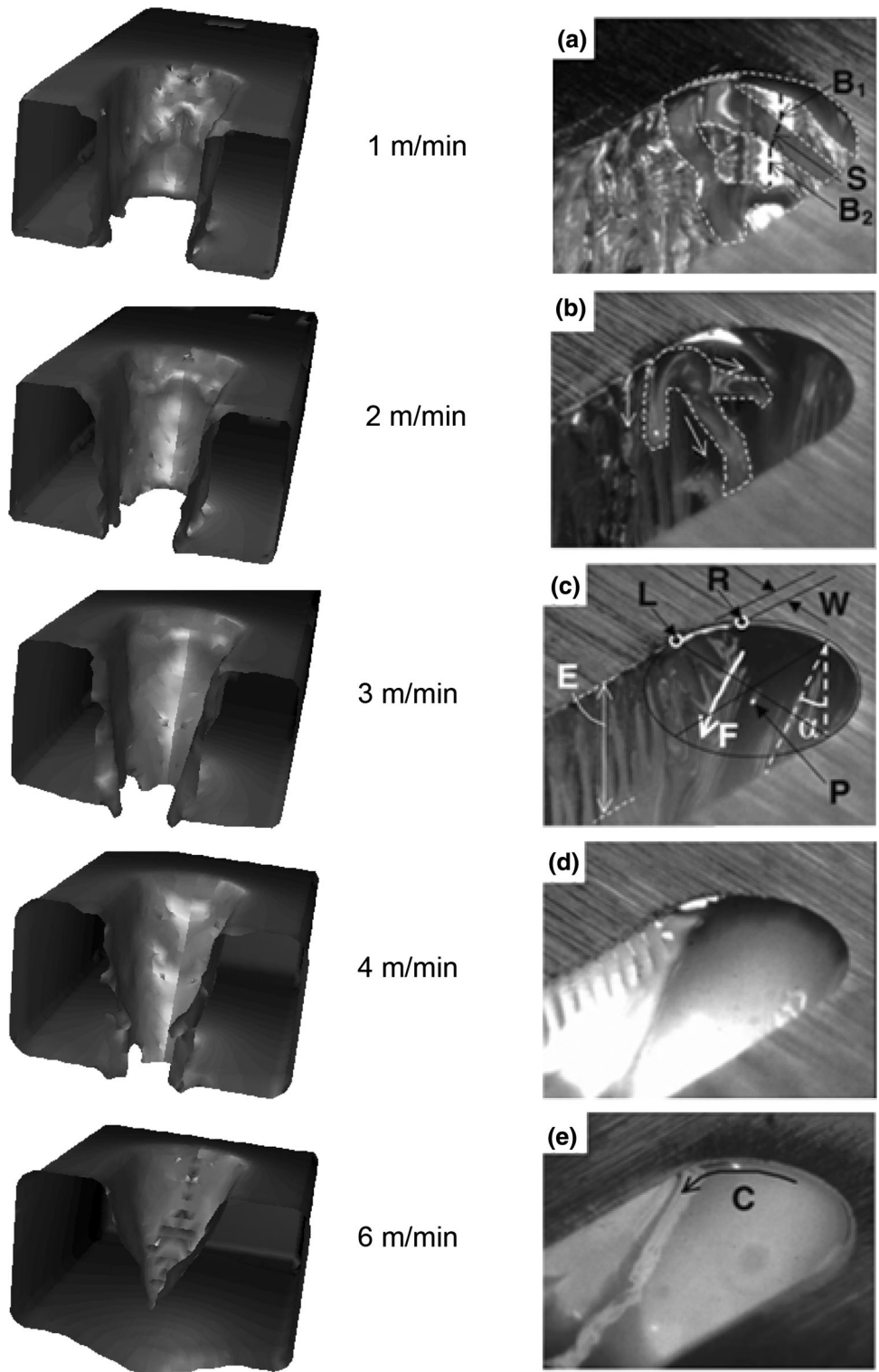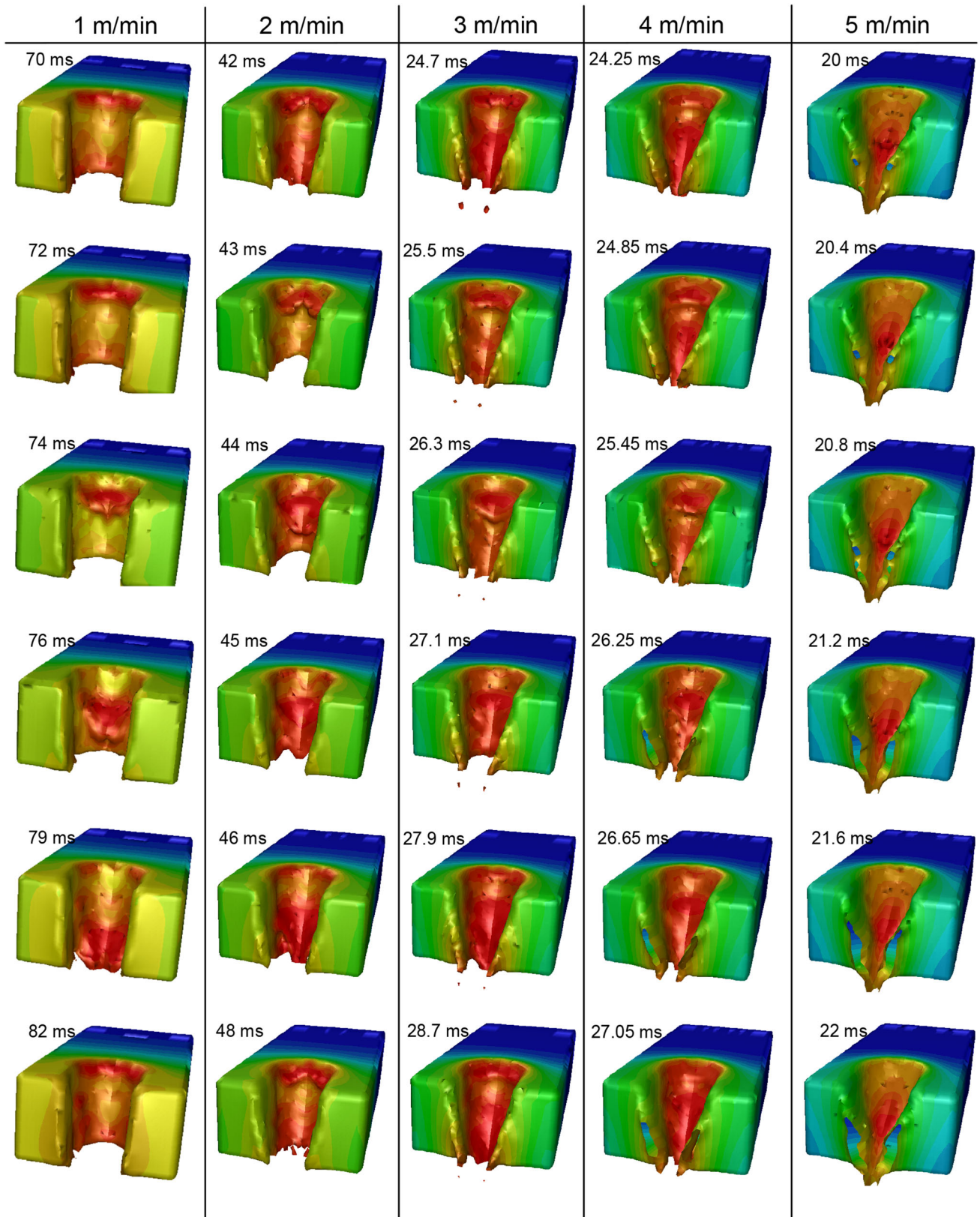
Fig. 9 Periodicity of hump formation as a function of the cutting velocity
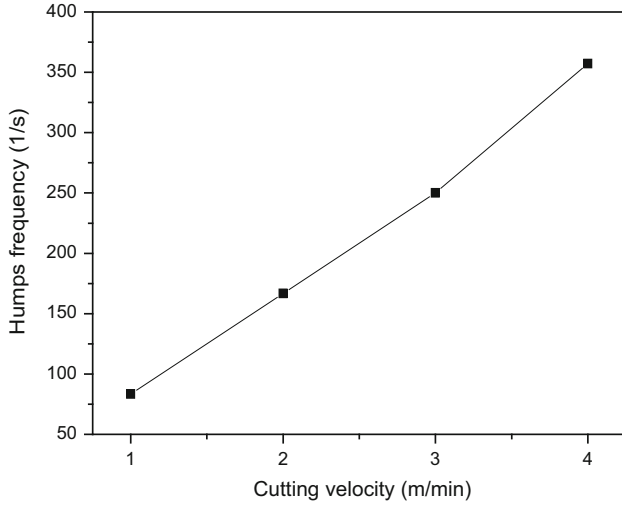
Fig. 10 Hump frequency as a function of the cutting velocity

$\rho(T) = -0.4522\,T + 7755.7\left[\text{kg/m}^3\right]$

$C_p(T) = 2.6137 \times 10^{-4}\,T^2 + 1.203462 \times 10^{-1}\,T + 124[\text{J/kg/K}]$

$K(T) = 76.307 - 0.0218\,T[\text{W/m/K}]\quad \text{if}\ T \geq T_F(=1808\,\text{K})$

$K(T) = 92.225\ \text{W/m/K}\quad \text{if}\ T < T_F$

The outflow boundary conditions are considered over all faces surrounding the air region, whereas the initial temperature is fixed at 300 K.

The calculation field is firstly obtained by the mean of the preprocessor Gambit (associated with Fluent solver), where the geometry and the mesh of the domains are defined.

Figure 4 shows the calculation domain containing the air and the sample regions. The sample is moved under the laser beam, the effect which is simulated through a source term inserted in the energy conservation equation.

The area under consideration is shown in Fig. 5. The total size of the calculation field composed of the air and the metallic sample is (10 mm × 4 mm × 4 mm), where $x_{\min} = 0$, $x_{\max} = 10$ mm, $y_{\min} = -2$ mm, $y_{\max} = 2$ mm, $z_{\min} = -3.5$ mm, $z_{\max} = 0.5$ mm. The size of the processed sample is (7.5 mm × 3.6 mm × 3 mm). Its initial position in the calculation field is determined such as: $x_{\min} = 2$, $x_{\max} = 9.5$ mm, $y_{\min} = -1.8$ mm, $y_{\max} = 1.8$ mm, $z_{\min} = -3$ mm, $z_{\max} = 0$ mm.

The 3D structured mesh of the calculation domain is shown in Fig. 6. It is composed of 19,800 hexahedral cells and 61,650 quadrilateral faces. The green mesh represents the workpiece, whereas the red one contains the cell for the air region. Along the y direction, the number of grid nodes is 41, and the magnitude of the step is 0.1 mm (100 μm). Along z direction, we have 31 grid nodes, and the magnitude of the step is 0.13 mm (130 μm). On the x direction, the min value of the grid is 0.1 mm (100 μm), and the max is 1 mm.

The advantage that the used structured grid has over unstructured one is a better convergence and a higher resolution. For an equivalent cell amount, the solution in hexahedral grid has highest accuracy. The mesh density must be sufficiently high in order to record the flow features, and in some regions, it should not be so high that it captures unnecessary details of the flow, leading to misuse of CPU and to time wasting.

To check the accuracy of the grid, we have performed an adaption of grid where the grid has been refined by dividing one hexahedron cell into eight ones. The calculation for the used grid and the refined one is represented in Fig. 7 for fixed time t. The figure gives the results of temperature profiles in the direction x for two depths following the z direction. The figure shows a quite nice accordance of temperatures obtained from the two grids at the depths $z = -0.5$ mm and $z = -0.1$ mm near the sample surface. To simulate the relative movement of the workpiece under the laser beam and inside the surrounding air, we consider the fact that by default, the solver Fluent calculates the equations of fluid flow and heat transfer, in a stationary or inertial reference frame. Therefore, in the case of laser cutting, in order to avoid a displacing source, we rather consider a displacement of the workpiece by solving the equations in a moving (or noninertial) reference frame. Such problems typically involve moving parts, and it is the flow around these moving parts that is of interest.

In the following, we present the comparison between the experimental observations and our numerical approach results concerning the dependance of the cutting front profile on the cutting velocity. The images shown in the right side of Fig. 8 are reported by Hirano and Fabbro [22] from their experiments.

A high-speed camera has been used to take pictures of the cutting front for different cutting velocities v_c varying from 1 to 6 m/min. It can be observed that the liquid flowing on the kerf front exhibits a strong dependence on v_c. It is clearly noted that for the both experimental and theoretical approaches, the results show quite interesting similarities concerning the melt behavior since the more the velocity is, the more the thin film flow tends to be laminar. It is also remarked that the striations are more important at low cutting speeds and tend to be reduced at higher speeds. We give in Fig. 9 the dependance on the cutting velocity of the hump formation periodicity.

It is clearly shown from Fig. 10 that at low velocities, the hump frequency is much more lower than at higher velocities, where the melt film flow tends to be laminar.
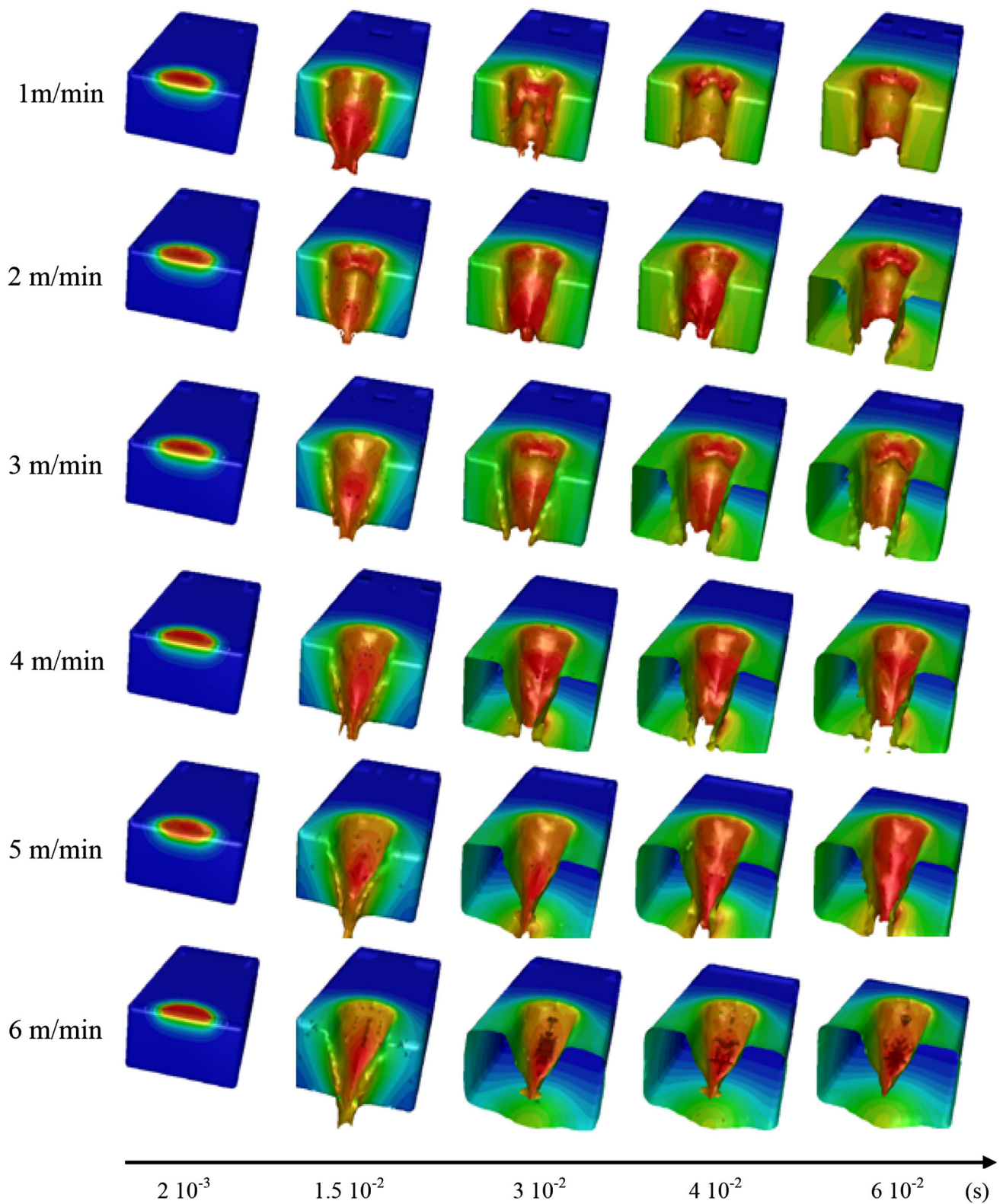
The agreement of such experimental results with our numerical model allows us to consider the developed modeling as a basis to propose a parametrical study of the metallic liquid behavior following the cutting speed.
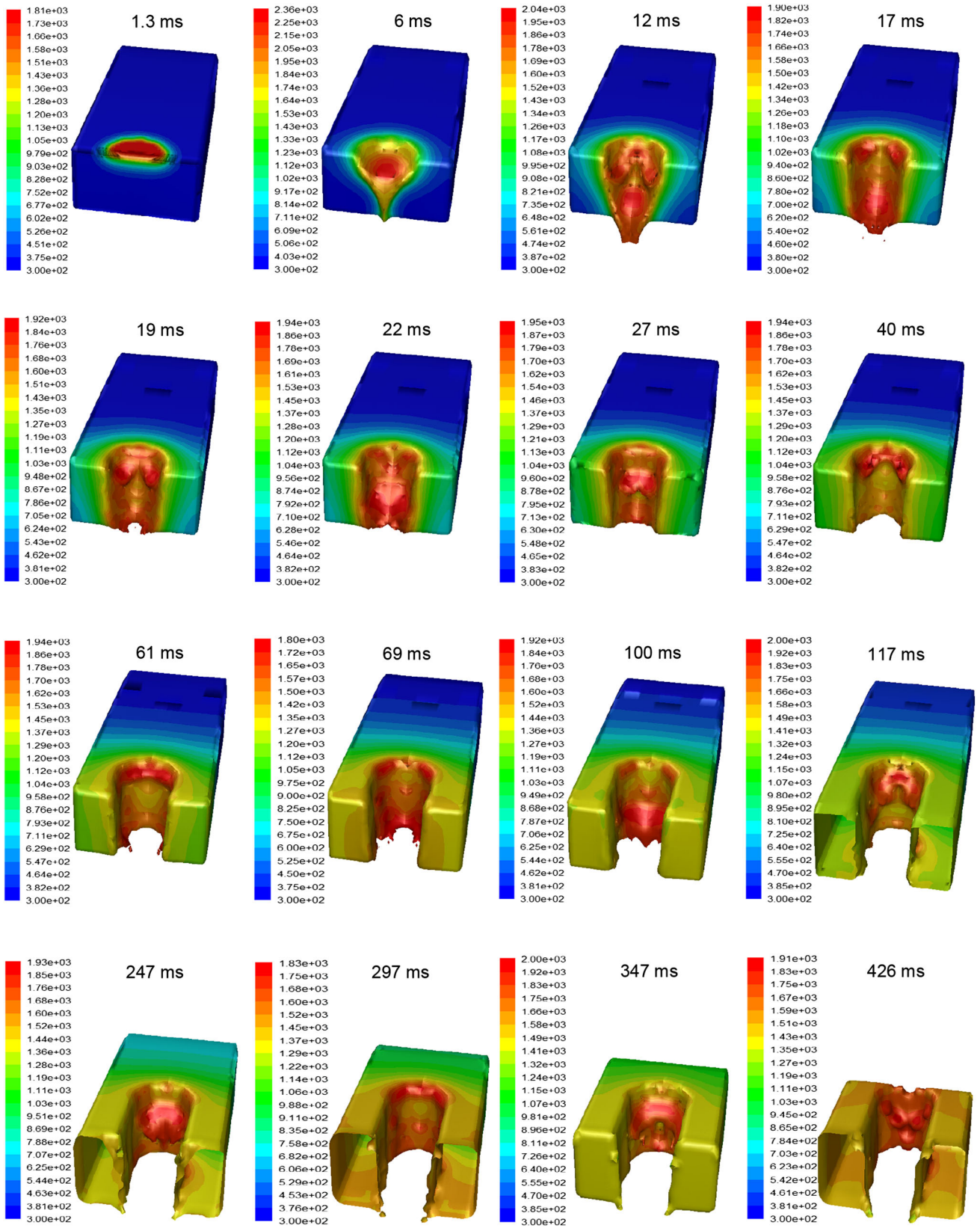
Fig. 11 Evolution of cutting front temperature field, and hump formation for a cutting velocity of 1 m/min

Fig. 12 Evolution of the liquid melt layer on the kerf front at different cutting velocities

Firstly, we emphasize in our study on the low cutting speeds for which the metallic liquid movements result in complex flow, characterized by melt accumulation where shelf structure observed by Golubev [15], Hirano and Fabbro [22], Hirano [27] appears on the top of the kerf and moves downwards while the workpiece is cut. This
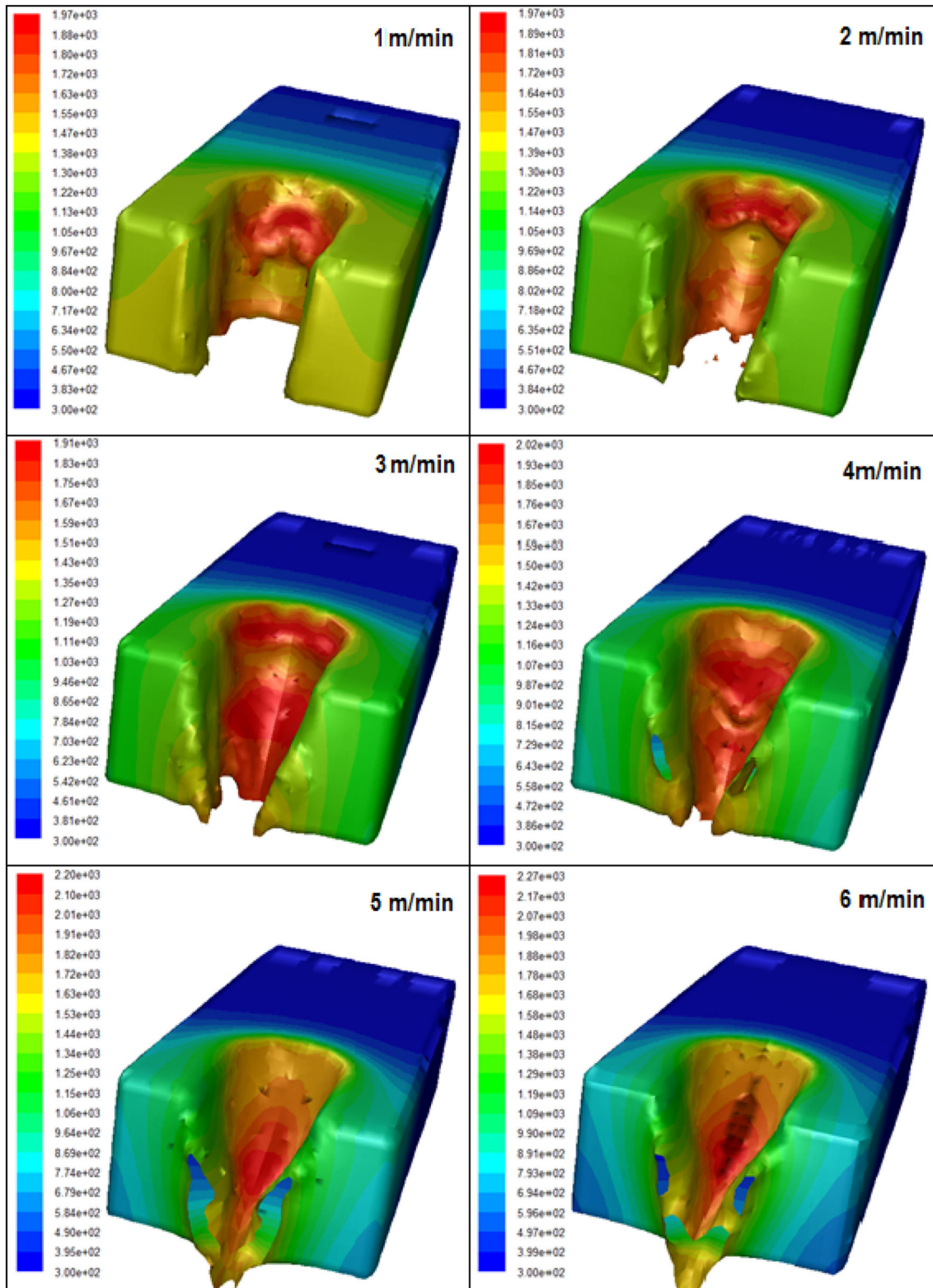
Fig. 13 Evolution of the temperature fields at different cutting velocities

mechanism is simulated by our numerical model, as it is shown in Fig. 11 for a cutting velocity equal to 1 m/min. It is noted that in this cutting velocity regime, a steep kerf front profile is exhibited and that the liquid dynamic is characterized by the periodical formation of humps moving on the kerf front toward the workpiece bottom, while the

workpiece is displaced at the cutting velocity under the laser beam. Moreover, concerning the temperature field distribution, we note as shown in the reported sequences, in the second frame of Fig. 11, that the maximum reached temperature is 2360 K. This allows us to comfort the assumption that the vaporization and plasma formation are not considered in our model for the used laser beam parameters, since the vaporization temperature for iron is about 2800 K. It can be deduced from the observation of the sequences that the occurring complex melt dynamics resulting from the periodical heating of the top surface of the humps, combined to the movement of the workpiece, could lead to the formation of striations observed on the lateral walls.

The results concerning the effect of the cutting velocity on the melt film dynamics are given in Fig. 12. Sequences corresponding to the same simulation times are represented for velocity varying from 1 to 6 m/min. It is clearly observed that the kerf front tilt angle increases with the velocity, and in the extreme case of 6 m/min, the inclination is so important that the workpiece is not cut entirely over its thickness. This fact was also confirmed in the experimental approach reported by Hirano and Fabbro [22] and Hirano [27] at such cutting velocity regime. At cutting velocity of 1 m/min, we note the occurence of humps which characterizes the absorption of the laser beam at different stages of the workpiece displacement. The humps tend to disappear for cutting speeds higher than 3 m/min, to reach a laminar regime of the melt flow at cutting speeds greater than 4 m/min.

With the laminar flow, we can also note the reduction of striations resulting from the increase in the velocity. It can be concluded that to obtain cuts without hump formation and consequently with reduced striations, it should be more interesting to proceed at higher velocities, but this is applicable mainly for thinner plates, as it is observed in many experimental works.

The temperature field at different laser cutting velocities is presented in Fig. 13. The figures are taken at approximately the same positions following x direction, for of course different times related to the displacement velocities. It is noted that the maximum temperature decreases with the cutting velocity. Typically, for velocities varying from 6 m/min to 1 m/min, the maximum temperature decreases from 2270 to 1970 K. Indeed, the laser beam covers a wider area on the workpiece due to the inclination of the cutting front, and accordingly the incident intensity on the surface: I_o cos (θ), increases as well. One can conclude that when the cutting velocity is higher, more absorption of laser energy occurs and thus more thermal conversion effect is obtained.

4 Conclusions

In our contribution on laser cutting study, we have developed a 3D numerical model to simulate the cutting front phenomena and kerf formation. The main features of the model appear through the use in the governing equations, source terms representing the incidence angle-dependent laser energy, the dynamic pressure gradient, and shear stress force effects. Quite good accordance with the experimental observations was obtained, allowing us to propose some interpretations on the effect of the process velocity in laser metal cutting. The developed model is a preliminary study which would allow us to go into more detailed comparisons with the experimental works and to study the effect of the main parameter variations.

In future, the model can be extended to the study of the evolution of the final roughness which appears on the lateral walls and determines the cut quality. The cut thickness and the wall roughness are indeed of great interest for the industry. The effect of many operating parameters can be studied, in particular the laser wavelength whose the crucial role is admitted in laser cutting, beside the parameters related to the treated materials such as thermo-physical properties or viscosity dependence with the temperature.

References

1. N.B. Dahotre, S.P. Harimkar, *Laser Fabrication and Machining of Materials* (Springer, New York, 2008)
2. J.F. Ready, *Industrial Applications of Lasers* (Academic Press, San Diego, 1997)
3. D. Schuocker, Appl. Phys. B **40**, 9 (1986)
4. D. Schuocker, P. Muller, Proc. SPIE **801**, 258 (1987)
5. W. Schulz, G. Simon, H.M. Urbassek, I. Decker, J. Phy. D Appl. Phys. **20**, 481 (1987)
6. M. Vicanek, G. Simon, J. Phys. D Appl. Phys. **20**, 1191 (1987)
7. M. Vicanek, G. Simon, H.M. Urbassek, I. Decker, J. Phys. D Appl. Phys. **20**, 140 (1987)
8. D. Petring, P. Abels, E. Beyer, Proc. SPIE **1020**, 123 (1988)
9. W. Schulz, D. Becker, Proc. European Scientific Laser Workshop on Mathematical Simulation (Lisbon, 1989)
10. N.K. Makashev, E.S. Asmolov, V.V. Blinkov, A. Yu Boris, O.G. Buzykin, A.V. Burmistrov, M.R. Gryaznov, V.A. Makarov, Sov. J. Quant. Elect. **22**, 847 (1992)
11. N.K. Makashev, E.S. Asmolov, V.V. Blinkov, A. Yu Boris, A.V. Burmistrov, O.G. Buzykin, V.A. Makarov, Proc. SPIE **2257**, 2 (1994)
12. A.F.H. Kaplan, J. Appl. Phys. **79**, 2198 (1996)
13. B.S. Yilbas, Heat Mass Transf. **32**, 175 (1997)
14. G. Tani, L. Tomesani, G. Campana, Appl. Surf. Sci. **208–209**, 142 (2003)
15. V.S. Golubev, Eprint No. 3 (ILIT RAS, Shatura, 2004)
16. B.S. Yilbas, B.J. Abdul Aleem, J. Phys. D Appl. Phys. **39**, 1451 (2006)
17. L.M. Wee, P.L. Crouse, L. Li, Int. J. Adv. Manuf. Tech. **36**, 699 (2008)

18. S.R. Rajpurohit, D.M. Patel, Int. J. Eng. Res. Appl. **2**(2), 457 (2012)
19. D. Teixidor, J. Ciurana, C.A. Rodriguez, Int. J. Adv. Manuf. Tech. **71**(9–12), 1611 (2014)
20. A. Otto, M. Schmidt, Phys. Procedia **5**, 35 (2010)
21. S. Kohl, M. Schmidt, Proc. ICALEO'2013, Miami, Florida, USA (Laser Institute of America, USA, 2013)
22. K. Hirano, R. Fabbro, J. Phys. D Appl. Phys. **44**, 105502 (2011)
23. C.W. Hirt, B.D. Nichols, J. Comput. Phys. **39**, 201 (1981)
24. A.V. Zaitsev, O.B. Kovalev, A.M. Orishich, V.M. Fomin, Quant. Elec. **35**, 200 (2005)
25. D.R. Lide, *CRC Handbook of Chemistry and Physics*, 84th edn. (CRC Press LLC, Boca Raton, 2004)
26. J.U. Brackbill, D.B. Kothe, C. Zemach, J. Comput. Phys. **100**, 335 (1992)
27. K. Hirano, PhD Thesis (ENAM, ParisTech, 2012)
28. J.H. Rasheed, J. Diyala, Pure Sci. **9**, 14 (2013)
29. W. Sutherland, Philos Mag. **36**(5), 507 (1893)
30. V.R. Voller, M. Cross, N.C. Markatos, Int. J. Num. Meth. Eng. **24**, 271 (1987)
31. V.I. Mazhukin, A.A. Samarskii, Surv. Math. Ind. **4**, 85 (1994)
32. E. Toyerskani, A. Khajepour, S. Corbin, Proc. ICALEO'2012, Scottsdale, Arizona, USA (Laser Institute of America, USA, 2002)
33. W.W. Duley, *CO_2 Lasers: Effects and Applications* (Academic Press, London, 1976), pp. 132–135
34. C. Lampa, A.F.H. Kaplan, M. Resch, C. Magnusson, Lasers Eng. **7**, 241 (1998)